

Charge trap identification for proton-irradiated p+ channel CCDs

Nick J. Mostek, Christopher J. Bebek, Armin Karcher, William F. Kolbe, Natalie A. Roe,
Jonathan Thacker

Lawrence Berkeley National Laboratory, Berkeley, CA, 94720, USA

ABSTRACT

Charge trapping in bulk silicon lattice structures is a source of charge transfer inefficiency (CTI) in CCDs. These traps can be introduced into the lattice by low-energy proton radiation in the space environment, decreasing the performance of the CCD detectors over time. Detailed knowledge of the inherent trap properties, including energy level and cross section, is important for understanding the impact of the defects on charge transfer as a function of operating parameters such as temperature and clocking speeds. This understanding is also important for mitigation of charge transfer inefficiency through annealing, software correction, or improved device fabrication techniques. In this paper, we measure the bulk trap properties created by 12.5 MeV proton irradiation on p+ channel, full-depletion CCDs developed at LBNL. Using the pocket pumping technique, we identify the majority trap populations responsible for CTI in both the parallel and serial transfer processes. We find the dominant parallel transfer trap properties are well described by the silicon lattice divacancy trap, in agreement with other studies. While the properties of the defects responsible for CTI in the serial transfer are more difficult to measure, we conclude that divacancy-oxygen defect centers would be efficient at our serial clocking rate and exhibit properties consistent with our serial pocket pumping data.

Keywords: Proton Radiation Damage, Silicon CCD Detectors, Pocket Pumping, Charge Transfer Efficiency

1. INTRODUCTION

The effect of charge transfer inefficiency (CTI) is a major source of performance degradation in silicon charge-coupled devices (CCDs). Large-format CCDs with millions of pixels typically require thousands of transfers to move collected charge from the imaging region to the output amplifier. Even a small CTI can result in a substantial fraction of the collected charge being deferred into the pixels directly following the initial charge collection location. The functional form of this deferred charge is given by:

$$F_{def} = CTE^N, \quad (1)$$

where F_{def} is the fraction of charge that is deferred, or lost from the pixel where it was originally deposited, N is the number of pixel transfers and $CTE = 1 - CTI$ is the charge transfer efficiency. The deferred charge shows up as a trail following the main charge packet, and results in degraded image resolution and decreased photometric accuracy. For example, if $CTE = 0.9999$, almost 10% of the charge will be deferred after 1000 transfers.

In space applications where diffraction-limited seeing is paramount, it is especially important to minimize CTI so as not to degrade the precise astrometry, photometry, and source shape measurements enabled from space. Advances in CCD design and fabrication ensure that devices can be constructed with very few charge trapping regions and hence low CTI, typically $< 10^{-5}$. For example, the buried channel process was developed to minimize the number of traps that are created by lattice mismatch between the silicon channel and epitaxial layers of surface channel CCDs, and the use of notched channels minimizes the number of traps encountered by small charge packets.

While CCDs may initially be produced with excellent CTE, charge trapping defects can be introduced into the silicon lattice by radiation. In particular, the low-energy protons (< 50 MeV) that are prevalent in the space

N. Mostek is co-affiliated with the Space Sciences Laboratory, University of California, Berkeley, CA, 94720, USA. He is based out of Lawrence Berkeley National Laboratory (telephone: 510-486-7595, email: njmostek@lbl.gov).

environment are particularly effective at creating traps as they collide elastically with silicon atoms and displace them from the lattice. The single silicon vacancy hole defect is mobile within the lattice and free to find stable configurations with other vacancies, creating divacancy traps (V_2). Alternatively, these vacancies can settle into new lattice locations by bonding with impurities within the silicon and creating new defects with different charge trapping properties. An example of this bonding is the phosphorus-vacancy (PV) defect common in proton damaged n-channel devices.¹ Any disruption to the pure silicon lattice creates potential wells for electrons (or holes) to be trapped and can therefore adversely effect the CTI of the device.²

A notable example of degraded CCD performance in a space environment comes from the Hubble Space Telescope (HST). Over the operating lifetime of HST, the CTE has degraded substantially for all flight CCD devices.³ For example, the 2010 projected photometric correction for CTE losses in the Advanced Camera for Surveys Wide Field Camera (ACS WFC) could range between 0.06 to 0.65 magnitudes, depending on the observing conditions. Such large corrections leads to systematic errors of 0.02-0.03 mag.^{4,5} In the context of cosmology, the flux correction for a $z = 1.5$ Type Ia supernovae at peak brightness will be ~ 0.12 mag, and therefore these corrections can impart significant errors to the photometric measurement of SNe luminosity. In addition to photometric corrections, recent efforts have been made to accurately characterize the CTI in ACS images to correct for charge trailing that distorts galaxy shapes and interferes with weak lensing measurements.⁶ The new software correction requires a model of the CTI which depends upon the aggregate properties of the radiation-induced trap populations present in the parallel and serial transfer processes. A more detailed knowledge of the radiation-induced defects in p-channel CCDs could enable the implementation of better correction algorithms for very precise galaxy shape measurements required for weak lensing studies.⁷

The experience to date with the CCDs flown on the HST strongly suggests that future space missions should employ CCDs with improved radiation tolerance, and that the properties of defects likely to be created while in orbit should be characterized so that the effects can be understood and corrected. In this paper, we will characterize defects due to low-energy proton irradiation in fully depleted p-channel CCDs developed at LBNL⁸ for the proposed Joint Dark Energy Mission (JDEM) satellite.⁹ These devices are fabricated on high-resistivity float zone n-type silicon and are significantly more radiation resistant than n-channel devices. Due to their increased radiation tolerance, previous studies have shown that the LBNL p-channel CCDs will suffer much less CTE degradation than the n-channel CCDs employed to date in space missions.^{10,11}

According to the Shockley-Hall-Read theory,^{12,13} the efficiency of charge trapping depends on the properties of the individual defect centers and the number of traps encountered during readout. The defects responsible for CTI in CCDs are characterized by their energy level in the band gap, E , and their capture cross section, σ_c . These parameters determine the emission time constant of the defect,¹ τ_e :

$$\tau_e(E, T, \sigma_c) = \frac{m_e}{\sigma_c} \frac{e^{E/(k_B T)}}{B m_{\text{eff}} T^2}, \quad (2)$$

In this equation, m_e , k_B , and m_{eff} are constants and will be discussed in more detail below. When τ_e is comparable to the pixel transfer time, it is most effective at contributing to increased CTI. Because τ_e is also a strong function of temperature, it is possible to determine σ_c and E by taking data with the CCD operated over a range of temperatures. To measure these parameters, we will use a technique called “pocket pumping” in which charge is shuffled back and forth between pixels many times to enhance the effect of charge trapping and reveal individual traps. By taking pocket pumping (PP) data over a wide range of temperatures, we can fit for the energy levels and cross-sections of the different trap populations.

This paper is organized as follows. In Section 2, we describe the low-energy proton irradiation and the PP technique. We detail our PP data analysis process and trap parameter fitting model in Section 3, and we investigate the trap annealing behavior in the both the parallel and serial transfer. In Section 4, we find the best fit parameters of the trap populations in our PP data for both the parallel and serial transfer directions. We also identify and discuss the displacement-damage defect species that are responsible for the majority of charge deferral given our CCD operating conditions. Our conclusions are presented in Section 5.

2. DATA

2.1 Proton Irradiation

To simulate the effects of low-energy proton irradiation, we used the LBNL 88-inch cyclotron BASE facility to irradiate three CCDs. The expected average proton displacement damage for the CCDs on the JDEM satellite in an L2 orbit is 6.6×10^6 MeV/g(Si), corresponding to 12.5 MeV proton fluence of 7.4×10^8 protons/cm².¹¹ In this experiment, we span a range of possible radiation doses from 5×10^8 - 1×10^{11} protons/cm² to demonstrate the CTI of the fully-depleted LBNL CCDs and to probe the trap characteristics. Table 1 lists the CCD types used in this work and the conditions for their proton irradiation. All CCDs were front-illuminated, 250 μ m thick devices with 3512×3512 pixels, 10.5 μ m pixel pitch, and four-corner readout. In addition, the LBNL CCD construction includes serial register pixels with three times the size of a imaging pixel, which allows for binning of charge on the device.

Table 1. List of CCD devices and measurement conditions for 12.5 MeV proton irradiation

Device	Metallization	Temperature	Total Dose
1	Aluminum	300K	$1.8 \times 10^{10}, 3 \times 10^{10}, 6 \times 10^{10}, 1 \times 10^{11}$ protons/cm ²
2	Aluminum	140K	$2 \times 10^8, 5 \times 10^8, 1 \times 10^9$ protons/cm ²
3	TiN	300K	$5 \times 10^9, 1 \times 10^{10}, 5 \times 10^{10}$ protons/cm ²

Device #1 was irradiated at room temperature with a high proton dose (1.8×10^{10} - 1×10^{11} protons/cm²). The device was left at room temperature for a full month before our testing, allowing ample time for mobile traps to settle into stable configurations upon additional room temperature anneals. We irradiated each of the four quadrants with different cumulative proton doses by mounting a 1/4 inch aluminum plate in front of the CCD quadrants after the desired dose level was achieved, effectively shielding the quadrant from further proton damage. We used the same shielding procedure on the second CCD (#2), which was mounted inside a cryogenic vacuum dewar and operated at 140K during irradiation. The cold-irradiated device received three different cumulative doses across the four available quadrants spanning 5×10^8 - 1×10^9 protons/cm². These levels of proton irradiation are equivalent to 3 to 10 years of exposure in an L2 orbit for JDEM. After irradiation, device #2 was continually held at 140K for 10 days during initial testing and then annealed to room temperature to investigate the annealing properties of the device. Device #3, which underwent TiN metallization instead of the typical Al metallization process, was also warm irradiated with a range of proton doses similar to device #1. Though we report the CTI of devices all three devices, we focused our pocket pumping experiments on device #1 in this study.

2.2 Charge Transfer Inefficiency

We measured the CTI of the irradiated devices with Fe⁵⁵ x-rays and compared with previously reported CTI results for LBNL CCDs from an earlier silicon wafer production lot.¹¹ Since CTI depends on both temperature and transfer clock rate, we note that these CTI measurements were at 140K and a 100kpix/sec read out rate. We also use a three-phase clock transfer process with an asymmetric delay, which corresponds to transfer times of ~ 1 ms in the parallel direction and $\sim 1\mu$ s in the serial direction.^{1,14} Figure 1 shows the CTI results under these conditions. We find CTI performance consistent with Ref. 11, and both sets of CTI measurements show vastly improved performance over the HST n-channel ACS CCDs. We note that for total radiation doses below 1×10^9 , there is little charge transfer loss due to radiation-induced traps. The measured CTI values in this regime are consistent with the Fe⁵⁵ x-ray CTI measurement error of 1.5×10^{-6} .

We also report the radiation-induced CTI for a device #3 where the nominal aluminum metallization has been replaced with higher resistivity TiN material. Figure 1 shows that the TiN-metallized device had slightly worse CTI relative to the Al CCDs but still has excellent overall radiation tolerance.

In addition to the room-temperature irradiation and CTI measurement of device #1, we also performed a CTI measurement of the cold-irradiated device #2 both before and after a room-temperature anneal. The highest dose level for this study was 1×10^9 protons/cm², equivalent to 10 years in an L2 orbit for the JDEM satellite. The cold-irradiation experiment is much closer to actual space flight radiation conditions at L2, particularly

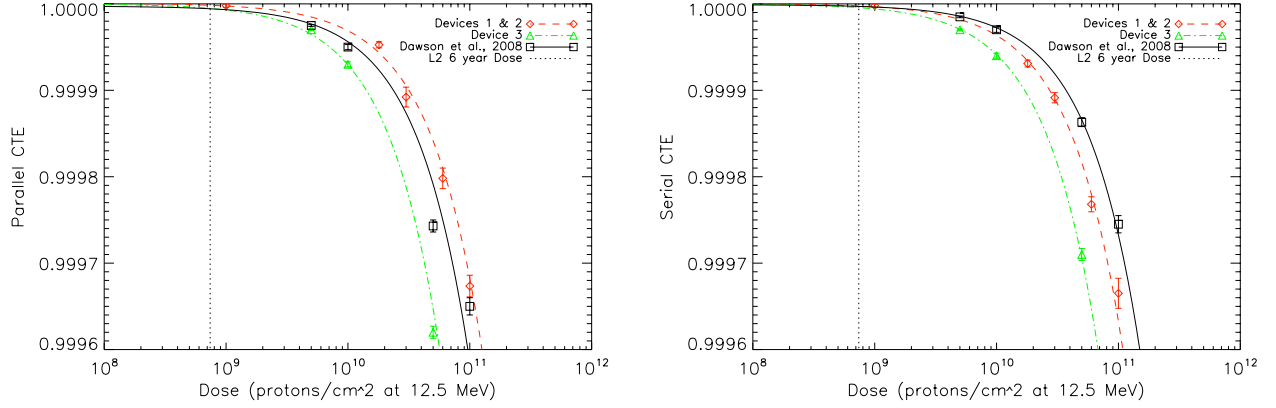


Figure 1. The parallel (left) and serial (right) charge transfer efficiency for the LBNL CCDs with aluminum metallization (red diamonds), TiN metallization (green triangles), and an aluminum-metallized CCD measured in Ref. 11. (black squares).

Table 2. CTI Measured from Al-metallized CCD with Fe^{55} x-rays at 140K

Dose (12.5 MeV protons/cm ²)	Annealed	Gain (ADU/e-)	Serial CTI ($\times 10^{-6}$)	Parallel CTI ($\times 10^{-6}$)
0	no	0.857	0.04 ± 1.2	2.2 ± 1.6
1×10^9	no	0.818	0.32 ± 1.3	2.4 ± 1.2
1×10^9	yes	0.810	4.3 ± 1.2	3.5 ± 1.5

when we consider the possible effects of onboard annealing procedures. Table 2 shows the measured Fe^{55} CTI for this device prior to irradiation, after irradiation, and following a single room temperature anneal cycle. We find very little change in the CTI after irradiation while operated constantly at 140K. However, we find a significant increase in serial CTI after a room-temperature anneal, consistent with the results of Ref. 11. We also find a small increase in the parallel CTI after anneal but the measured difference is within the margin of error.

2.3 Pocket Pumping

To determine radiation-induced trap characteristics, we use the PP technique. Beginning with an unsaturated flat field image on the CCD, the PP process repeatedly moves charge back and forth by one pixel in either the parallel or serial direction. As the flat field charge is transferred over a charge trap, charge is removed from the original charge packet and re-emitted according to the trap emission time constant into the following charge packet. As the original charge packet is repeatedly moved back and forth over the trap, additional charge is transferred to the trailing pixel in the transfer direction and leaves an excess of charge on one pixel and a depleted charge on the neighboring pixel. Therefore, the PP process creates a “dipole” signal relative to the flat image background, as seen in Figure 2. The order of the bright and dark pixel will depend on the clock phase location of the trap and the direction of charge transfer.

For the measurements reported here, we acquired PP data over a temperature range of 128K-210K in 5K increments. The PP process is performed using a pocket length of one pixel on a flat field image of several thousand electrons. The charge pumping is iterated for a number of cycles that provides a 3σ spike above the Poisson noise but does not fully deplete the total available charge within the charge packet in most cases.

3. ANALYSIS

3.1 Pixel-level Trap Efficiency

One way to look at the PP signal is through a histogram of the selected dipoles at each temperature. Figure 3 shows the number counts of the excess charge dipole locations as a function of “trap efficiency”, defined as the average amount of trapped charge per PP transfer cycle. The histogram shows the aggregate effect of deferring

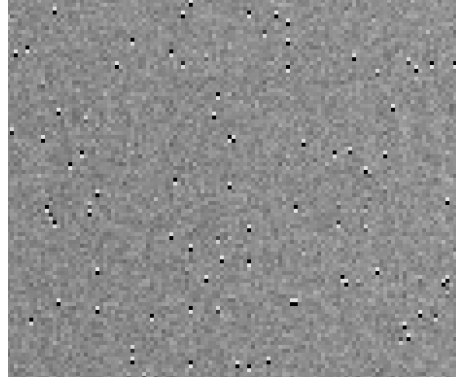


Figure 2. An example parallel pocket pumping image from device #2. Charge traps are identified with the characteristic “dipole” signal spike and depletion between two neighboring pixels.

charge into these single pixel locations at a given temperature. One can fit for the average value of these trap efficiency peaks and use that information to determine the global trap efficiencies and characteristics as a function of temperature.¹⁴

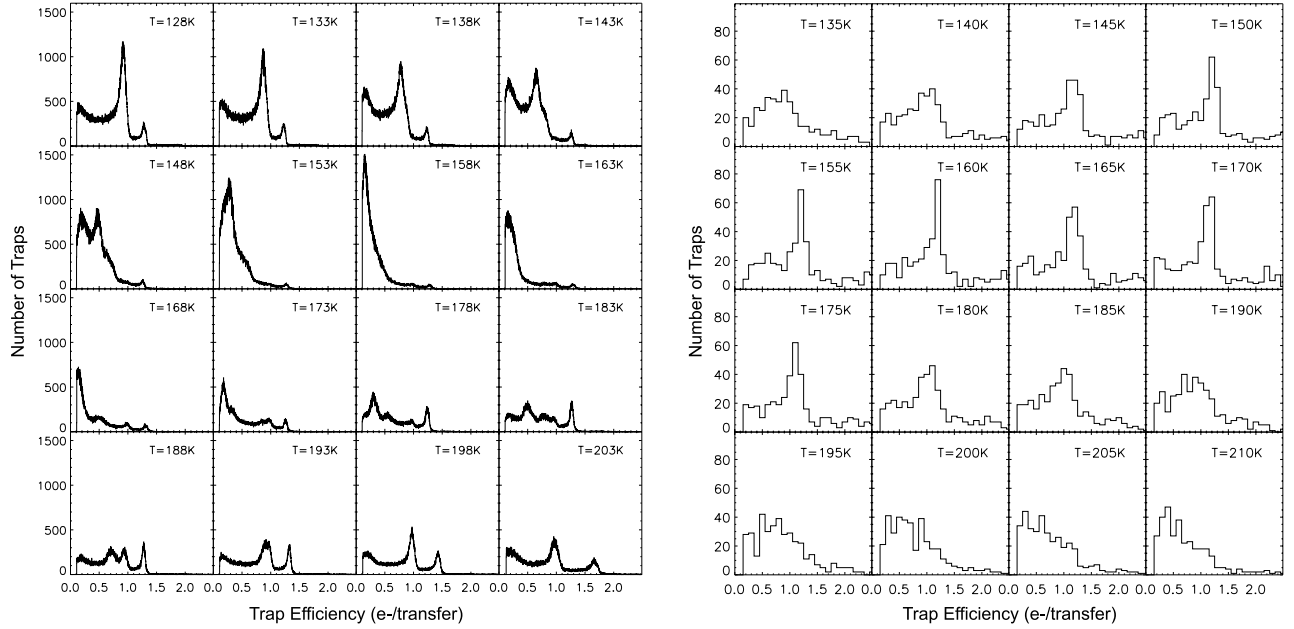


Figure 3. The parallel (left) and serial (right) trap efficiency histograms measured from pocket pumping. The trap efficiency is measured as the difference of the peak of the PP dipole signal from the mean flat field level divided by the number of PP cycles. Note that the parallel trap histogram shows a saturation peak at $\sim 1.5e^-$ / transfer when all of the available flat field charge has been transferred into the trap.

In order to better characterize the individual defect properties, we filter out the PP dipoles from the flat field image on a pixel-by-pixel basis and track the trap efficiency at each pixel location as a function of temperature. The actual trap pixel location is defined to be at the dipole peak pixel location. When selecting PP traps, we require that the traps be identified in a minimum of three pocket pump images at different temperatures with a $> 3\sigma$ detection above the flat field noise. This allows us to probe the specific trap characteristics at a specific pixel location as well to identify multiple traps within a specific location. However, the identification breaks down when the number density of traps per pixel becomes so high that traps occupy neighboring pixels, in which case the charge pumping across an individual pixel becomes an inaccurate measure the trap characteristics. For

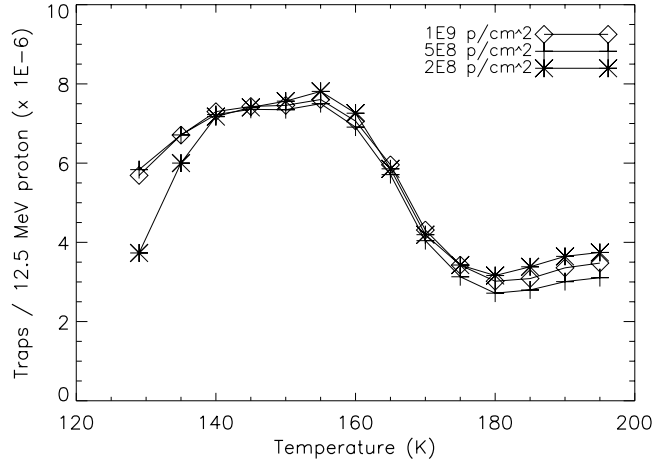


Figure 4. The number of detected parallel traps per delivered 12.5 MeV proton for all radiation doses on device #2.

this reason, a pixel-level PP analysis is best used when the trap number densities are low.

3.2 Density of Traps

In proton-irradiated devices, the CTI depends on the number of effective traps that are present in the charge transfer process at a given operating temperature. To show the relationship of the number of traps created for various levels of radiation, we simply count the total number of parallel traps that are effective above the 3σ detection limit in the flat-field Poisson noise. For these measurements, we used 10000 parallel PP transfers over one pixel with a mean flat field level of ~ 8000 electrons, resulting a 3σ detection limit of 0.027 electrons per transfer.

Figure 4 shows the number of parallel traps per incident proton detected at each of the radiation doses on device #2. By normalizing the number of traps by the number of delivered protons to the CCD, we see that the trap densities are consistent with one another, indicating that the number of traps scale linearly with proton dose. We also see that the overall number of traps changes with temperature, consistent with Figure 3. The observed maximum number of traps created for each delivered 12.5 MeV proton is $\sim 8 \times 10^{-6}$ traps per proton.

3.3 Trap Parameter Fitting

Radiation-induced defect centers defer charge according to the characteristic emission and capture time constants of the trap. These factors contribute to the trap efficiency for a given temperature and clock period. Using the PP technique, we measure the trap efficiency as a function of temperature and fit for the intrinsic defect parameters of the trap. The total charge transfer efficiency as a function of temperature is modeled with

$$CTI_{pp}(T) = \sum_i N_i M(\tau_e, \tau_c) \sum_{k=1}^3 F_{gk}(\tau_e, \tau_c) \quad (3)$$

where N_i is the number of trap defects of species i per pixel and $M(\tau_e, \tau_c)$ is the clock phase-independent trap efficiency written as

$$M(\tau_e, \tau_c) = \frac{\tau_e}{3(\tau_e + \tau_c)}. \quad (4)$$

The clock phase-dependent efficiency term $F_g(\tau_e, \tau_c)$ is the linear combination of the trap efficiency from each of the three clock phases (see Appendix of Ref 14 for complete description of these terms).

The CTI behavior depends heavily on the emission and capture time constants. The emission time constant is modeled with Eq. 2 where m_e is the electron mass, k_b is the Boltzmann constant, m_{eff} is the density of states

effective mass or $0.549 m_e$, $B = 3.256 \times 10^{21} K^{-2} cm^{-2} s^{-1}$, E is the activation energy of the defect center (or trap energy), and σ_c is the capture cross section of the trap defect. The capture time constant is given as

$$\tau_c(T, \sigma_c) = \frac{1}{\sigma_c n_d \sqrt{3 k_b \frac{T}{m_{eff}}}} \quad (5)$$

where n_d is the free electron density. To scale the electron density appropriately to our pocket pumping data, we compute n_d as the fractional volume of charge taken by a single electron in the pixel, computed as $n_d = 3.5 \times 10^{18} e^-/m^3$ for the parallel transfer and $n_d = 9.7 \times 10^{18} e^-/m^3$ for the serial transfer configuration. In both the serial and parallel cases, these free electron densities correspond to nearly-instantaneous capture time constants of $< 10^{-11}$ seconds over our range of temperatures and therefore has a negligible effect on the CTI at the typical 100 kHz clocking speed.

The model used in our analysis assumes that the PP data has been normalized to the trap efficiency defined in Sec. 3.1, thereby removing the detector gain, charge signal, and number of pumping cycles from the model. We formulate the χ^2 statistic

$$\chi^2 = \sum_{i=T_0}^{T_n} \frac{[CTI_m(T_i) - CTI_{pp}(T_i)]^2}{\sigma_d^2}, \quad (6)$$

where $CTI_{pp}(T)$ is calculated from Eq. 3, $CTI_m(T)$ is the observed charge loss per transfer as a function of temperature measured from the pocket pumping data, and σ_d is the 1σ Poisson noise of the flat field charge signal used in the pocket pumping measurement. The χ^2 is minimized for each pixel location using the IDL MPFIT routine, using the trap energy, cross section, and number of traps per pixel as free parameters for each fit defect type. We also require that each fit is performed over the same range of temperatures even though a given trap species may not be efficient at all temperatures. When a selected trap does not have a PP dipole signal $> 3\sigma$ above the flat field, we give that PP measurement less significance in the fit by assigning the trap signal a value of zero and an error of 3σ measured from the flat field noise.

4. DISCUSSION

4.1 Parallel Transfer Traps

Figure 5 shows 16 parallel transfer traps identified in CCD #1 after 12.5 MeV proton irradiation at 1.8×10^{10} protons/cm² total dose. The trap efficiency, as defined previously in Section 3.1, is plotted versus temperature with error bars measured from the 1σ Poisson noise of the flat field charge signal. A few interesting trends can be seen in the figure. Most of the traps have a peak efficiency (maximum loss of charge per transfer) near 140K, but a few other traps peak near 160K and 200K. In most cases, the trap efficiencies find a maximum loss of $\sim 1e^-$ /transfer. In a few pixels, multiple peaks in the trap efficiency are observed. Both the identification of multiple peaks and efficiencies greater than $1e^-$ indicate multiple defect centers per pixel. These cases compose a small fraction of the total traps induced at this radiation dose level.

To begin fitting the trap parameters with our χ^2 minimization, we input initial parameter values for the traps expected to be present during parallel transefer. The assumed active defects over the temperature range 125-210K correspond to the silicon divacancy (V_2), carbon interstitial (C_i), and carbon-oxygen (C_iO_i) hole traps.^{14, 15} The activation energies and cross sections for these traps are used as initial values to our fit as shown in Table 3. The trap parameters were also allowed to vary by $\pm 50\%$ in energy and a factor of four in cross section in the χ^2 minimization. The lines in Figure 5 show the best fit CTI based on the model described in Section 3.3, and we find that the range of values allowed generally fits the data with $\chi^2/Dof \sim 1$. We explicitly reject fits with $\chi^2/Dof \geq 2.5$ and any fits where the χ^2 minimum is at the parameter limits. These data cuts ensure a proper goodness of fit for our identified trap sample.

Figure 6 shows the histograms of trap activation energies and capture cross sections by fitting the PP data from 5×10^5 pixels on the device #1 quadrant irradiated with 1.8×10^{10} dose. The large peak in fitted energies and cross sections shows that the divacancy trap is clearly the dominant defect for parallel transfer in the LBNL p-channel devices, followed by the carbon-oxygen defect and the carbon interstitial. Since this device was irradiated

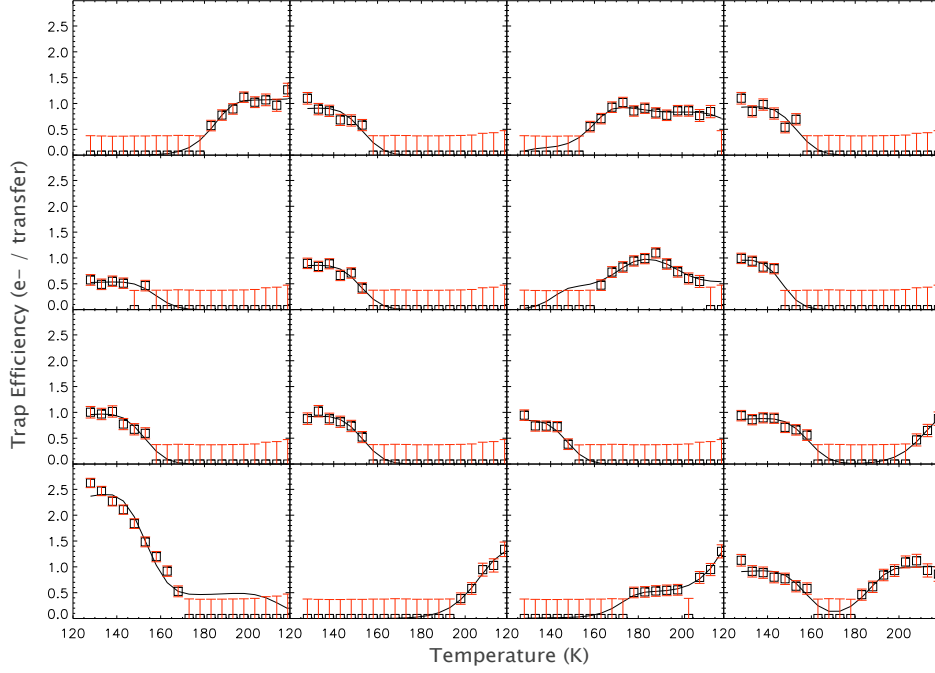


Figure 5. A random sample of identified parallel traps in the pocket pumping data. The black line shows the minimum χ^2 fit for each trap site. When the trap is not detected at a specific temperature, we explicitly set the trap efficiency to zero and assign an error of 3σ from the flat field Poisson noise.

Table 3. Hole Trap Parameters for Parallel Pocket Pumping Fit at 1.8×10^{10} protons / cm^2 Dose

Defect	Input E (eV)	Input $\text{Log}(\sigma_c)$ (cm^2)	Fit E (eV)	Fit $\text{Log}(\sigma_c)$ (cm^2)
V_2	0.21	-15.1	0.184 ± 0.012	-15.0 ± 0.3
C_i	0.28	-14.4	0.287 ± 0.068	-14.5 ± 0.4
C_iO_i	0.34	-14.6	0.388 ± 0.040	-14.6 ± 0.4

warm and allowed to anneal at room temperature, we would expect that carbon interstitial defects created in the proton irradiation would be mobile over this period and would settle into more stable configurations with pre-existing bulk oxygen atoms such as C_iO_i and leaving very few C_i defects in the silicon lattice. It is clear from Figure 6 that the trap cross section is more difficult to constrain than the trap energy with the existing data. The inaccuracy of the cross section fit is likely due to the dependencies in the emission time constant. Equation 2 shows that τ_e is exponentially dependent on E but linearly dependent on σ_c , providing a larger lever arm in determining the trap energy over the trap cross section.

Table 3 records the fitted E and σ_c values for each defect type. The trap energies and cross sections fit from our data are consistent with the initial assumed values taken from the literature within the RMS errors, confirming that the three chosen traps types are responsible for the majority of defects present in our PP data. Using the mean best fit trap parameters for each species, the trap efficiency temperature dependence is shown in Figure 7.

4.2 Serial Transfer Traps

Since the transfer rates in the serial register are over three orders of magnitude faster than the parallel transfer rate, defects with much shorter emission time constants become effective at deferring charge in the serial direction. Conversely, the same defect centers that are effective for the parallel transfer will have emission time constants that are longer than an entire read of the serial register. For example, applying the serial transfer rate and density of states to Equation 3 predicts that the V_2 trap efficiency cannot contribute more than $0.1e^-/\text{transfer}$ to the CTI, a decrease of a factor of 10 over the peak parallel trap efficiency.

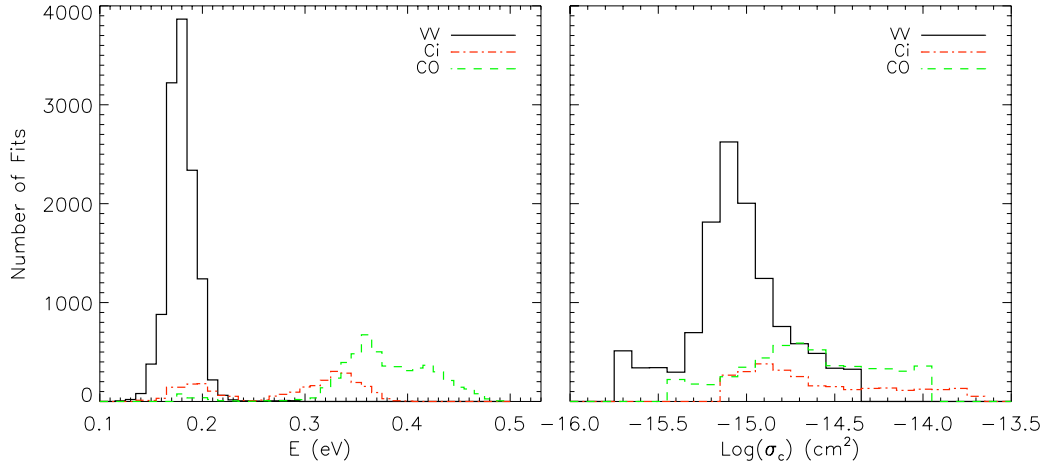


Figure 6. The distribution of best fit parallel trap parameters by allowing three trap species per pixel. The initial defect parameter values correspond to the silicon divacancy V_2 (black, solid), the carbon interstitial C_i (red, dot-dashed), and the carbon-oxygen interstitial C_iO_i (green, dashed). The mean best fit parameter values and errors are reported in Table 3.

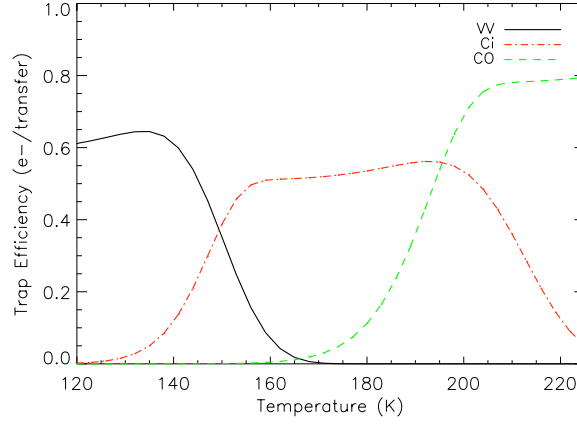


Figure 7. The modeled trap efficiencies for the parallel trap defects using the fitted values for E and σ_c shown in Table 3.

An additional complication to measuring serial trap efficiencies is that serial pocket pumping has 1/1750 of the total CCD pixels in which to probe the trap identities. However, our pixel-by-pixel analysis of temperature-dependent PP data allows us to identify individual trap defect centers and therefore learn the identity and characteristics of serial trap sites. Figure 8 shows a snapshot of 16 traps identified in the serial transfer register of the warm-irradiated CCD #1. Unlike the parallel PP data in Figure 5, the serial PP data seems to be more homogenous from pixel to pixel with a single trap efficiency temperature dependence that peaks at $\sim 175\text{K}$.

To fit the serial PP data, we repeated the procedure from the parallel transfer by modeling the trap efficiencies and time constants using Equations 2 and 5 and fitting the observed charge loss per transfer. The CTI model is identical to the parallel transfer except that we modify the pixel volume size due to the serial register geometry and account for the faster clocking periods. In the case of the serial transfer, we have no *a priori* knowledge of the trap species that may be efficient for the serial configuration. Therefore, we have not assumed initial parameter values associated with particular trap species but rather allowed a fit over a wide range of trap energies and cross-sections ($E = 0.25 \pm 0.15$ and $\text{Log}(\sigma_c) = -13.4 \pm 2.3$).

Compiling all of the best fit parameters ($\chi^2/\text{Dof} < 2.5$ and removing fits at the parameter fitting limits), Figure 9 shows the trap parameters that describe the charge deferral in the serial transfer. We find that 97% of

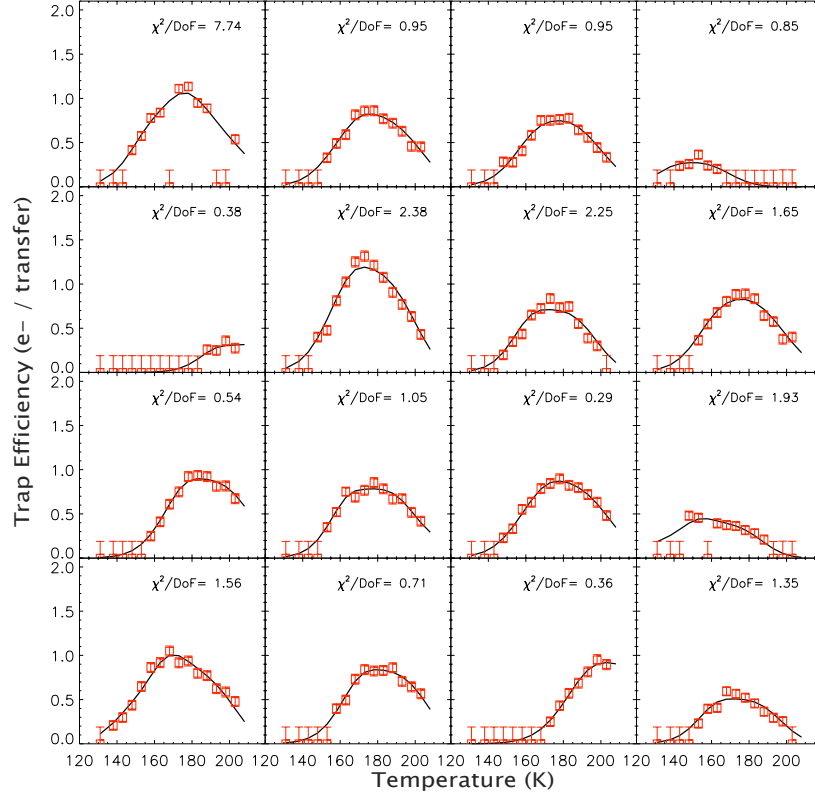


Figure 8. A sample of 16 serial traps identified and measured in our pocket pumping data. We note that the majority of traps have the same temperature dependence, which indicates a single population of trap defects.

the traps can be fit with $\chi^2/\text{Dof} < 2.5$ and that a single trap species (dubbed the X defect) best represents the majority of the traps measured in the serial PP data. The fitted mean energy and cross section values for this trap are $E = 0.242 \pm 0.025$ and $\text{Log}(\sigma_c) = -13.3 \pm 0.4$. These fit values are consistent with previously reported values of $E = 0.24$ and $\text{Log}(\sigma_c) \sim -13$ for the V_2O hole defect.¹⁶

While the X defect is the most likely to be the dominant trap, it is possible that divacancy traps are a contributing source of serial charge deferral. Figure 10 shows the model trap efficiency temperature dependence using the best fit X defect parameter values and the V_2 trap parameter values fit from the parallel PP data. The figure shows that both sets of parameter values have a similar temperature dependence, but the divacancy trap has a much lower efficiency for trapping charge and therefore would require $\sim 10V_2$ traps to cluster within a single pixel to produce the observed $1e^-/\text{transfer}$ trap efficiencies. Given the *total* trap number density measured from the parallel PP data (see Section 3.2), we expect an upper limit of 1.4 traps per pixel for our serial test conditions. The probability that a cluster of 10 V_2 traps would randomly occur in the same pixel is $\ll 1\%$, and therefore we conclude that the V_2 trap *alone* could not explain the majority of $1e^-$ in the serial PP data.

5. CONCLUSION

In this paper, we have presented CTI measurements of the LBNL p-channel CCDs after 12.5 MeV proton irradiation. We have found that the overall CTI performance in both the parallel and serial transfer is in good agreement with previous studies. We also found that TiN metallization on these CCDs has very little effect on the CTI, with only a marginal increase at the very highest radiation doses above 1×10^{10} protons/cm².

By using a charge trapping model based on the Shockley-Hall-Read model and modified for the asymmetric, three-phase, 100 kHz clock timing, we have used the PP data to identify the types of trap defects created by

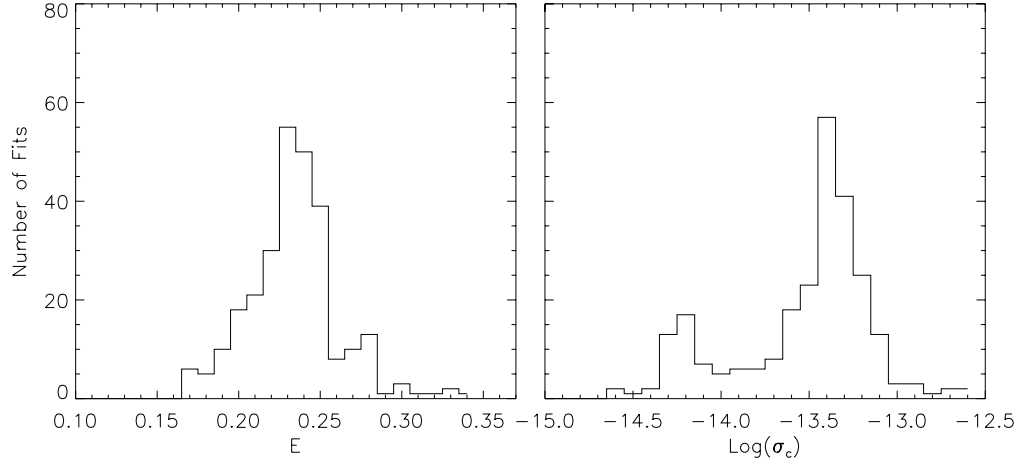


Figure 9. Best fit serial trap parameter values after removing fits with $\chi^2/Dof \geq 2.5$ and fitted parameter values at the parameter limits.

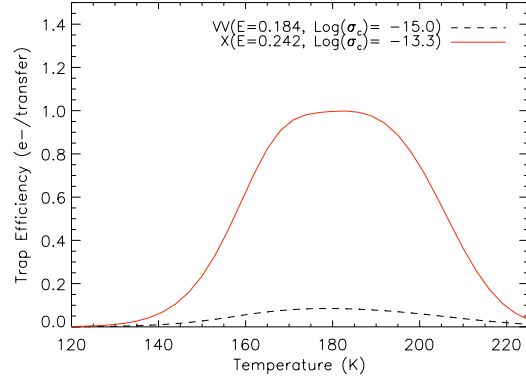


Figure 10. The model serial charge trap efficiency using the peak best fit values in Figure 9. Both model curves are normalized to one trap per pixel to show the difference in efficiency between trap species.

proton damage that affect CTI in the parallel and serial transfer directions. We found that the population of trap species in the parallel transfer is dominated by the silicon divacancy trap at the nominal 140K operating temperature. We also found evidence for the existence of the carbon-oxygen interstitial and carbon interstitial traps at higher temperatures even after a month of room-temperature anneal. These results confirm the previous parallel PP results for the LBNL p-channel CCDs presented in Ref. 14.

We also provide the first measurements of the serial trap defect population at the serial clock timing speeds for the LBNL p-channel CCDs. Through our model fitting analysis, we found that the majority of the serial traps can be described by a single defect with activation energy $E = 0.237$ eV and a capture cross section of $\sigma_c = 3.2 \times 10^{-14}$ cm². By restricting our model fit, we find that 97% of the measured post-anneal serial traps can be explained by the unidentified trap defect. We note that the best fit defect parameter values correspond to independently measured values for the V_2O complex. Additional analysis found that while the divacancy trap could have a temperature dependence that matches our data, the trap is very inefficient at the serial clocking speeds and requires an unphysical trap density per pixel to fit the data. Given that the V_2 defect is known to exist in high number densities in proton-damaged p-channel devices, we suspect that this unidentified species is related to V_2 through the V_2O complex.

ACKNOWLEDGMENTS

We would like to thank Steve Holland and Kyle Dawson for useful discussions. This work was sponsored by the United States Department of Energy under contract No. DE-AC02-05CH11231.

REFERENCES

- [1] Janesick, J. R., [*Scientific Charge-Coupled Devices (SPIE Press Monograph Vol. PM83)*], SPIE Publications (2001).
- [2] Srour, J., Marshall, C., and Marshall, P., “Review of displacement damage effects in silicon devices,” *Nuclear Science, IEEE Transactions on* **50**, 653 – 670 (Jun. 2003).
- [3] Sirianni, M. and Mutchler, M., “Radiation Damage in HST Detectors,” in [*Scientific Detectors for Astronomy 2005*], J. E. Beletic, J. W. Beletic, & P. Amico, ed., 171–+ (Mar. 2006).
- [4] Riess, A. and Mack, J., “Time Dependence of ACS WFC CTE Corrections for Photometry and Future Predictions,” tech. rep., Space Telescope Science Institute (May 2004).
- [5] Chiaberge, M., Lim, P. L., Kozhurina-Platais, V., Sirianni, M., and Mack, J., “Updated CTE photometric correction for WFC and HRC,” tech. rep., Space Telescope Science Institute (Apr. 2009).
- [6] Massey, R., Stoughton, C., Leauthaud, A., Rhodes, J., Koekemoer, A., Ellis, R., and Shaghoulain, E., “Pixel-based correction for Charge Transfer Inefficiency in the Hubble Space Telescope Advanced Camera for Surveys,” *MNRAS* **401**, 371–384 (Jan. 2010).
- [7] Rhodes, J., Leauthaud, A., Stoughton, C., Massey, R., Dawson, K., Kolbe, W., and Roe, N., “The Effects of Charge Transfer Inefficiency (CTI) on Galaxy Shape Measurements,” *PASP* **122**, 439–450 (Apr. 2010).
- [8] Holland, S. E., Bebek, C. J., Dawson, K. S., Emes, J. H., Fabricius, M. H., Fairfield, J. A., Groom, D. E., Karcher, A., Kolbe, W. F., Palaio, N. P., Roe, N. A., and Wang, G., “High-voltage-compatible, fully depleted CCDs,” *High Energy, Optical, and Infrared Detectors for Astronomy II* **6276**(1), 62760B, SPIE (2006).
- [9] Moos, W., Baltay, C., Benford, D., Bernstein, G., Freedman, W., Hirata, C., Kim, A., Kolb, R., Malhotra, S., Padmanabhan, N., Rhodes, J., Tarle, G., Gehrels, N., and Levi, M., “JDEM-ISWG Report to NASA and DOE Headquarters,” <http://jdem.gsfc.nasa.gov/> (May 2010).
- [10] Marshall, C. J., Marshall, P. W., Wacynski, A., Polidan, E., Johnson, S. D., and Campbell, A., “Comparisons of the proton-induced dark current and charge transfer efficiency responses of n- and p-channel ccds,” *Optical and Infrared Detectors for Astronomy* **5499**(1), 542–552, SPIE (2004).
- [11] Dawson, K., Bebek, C., Emes, J., Holland, S., Jelinsky, S., Karcher, A., Kolbe, W., Palaio, N., Roe, N., Saha, J., Takasaki, K., and Wang, G., “Radiation Tolerance of Fully-Depleted P-Channel CCDs Designed for the SNAP Satellite,” *Nuclear Science, IEEE Transactions on* **55**, 1725 –1735 (Jun. 2008).
- [12] Shockley, W. and Read, W. T., “Statistics of the Recombinations of Holes and Electrons,” *Phys. Rev.* **87**, 835–842 (Sep. 1952).
- [13] Hall, R. N., “Electron-Hole Recombination in Germanium,” *Phys. Rev.* **87**, 387 (Jul. 1952).
- [14] Bebek, C., Groom, D. E., Holland, S. E., Karcher, A., Kolbe, W. F., Lee, J. S., Levi, M. E., Palaio, N. P., Turko, B. T., Uslenghi, M. C., Wagner, M. T., and Wang, G., “Proton radiation damage in high-resistivity n-type silicon CCDs,” *Sensors and Camera Systems for Scientific, Industrial, and Digital Photography Applications III* **4669**(1), 161–171, SPIE (2002).
- [15] Moll, M., *Radiation Damage in Silicon Particle Detectors*, PhD thesis, Physics Dept., Univ. of Hamburg, Germany (1999).
- [16] Trauwaert, M. A., Vanhellemont, J., Maes, H. E., Bavel, A. M. V., Langouche, G., Stesmans, A., and Clauws, P., “Influence of oxygen and carbon on the generation and annihilation of radiation defects in silicon,” *Materials Science and Engineering B* **36**(1-3), 196 – 199 (1996). European Materials Research Society 1995 Spring Meeting, Symposium N: Carbon, Hydrogen, Nitrogen, and Oxygen in Silicon and in Other Elemental Semiconductors.